Thermal Structural Behavior of ElectrochemicallyLithiated Graphite (Li$_x$C$_6$) Anodes in Li-ion Batteries

Tobias Hölderle,[a, b] Mykhailo Monchak,[b, c] Volodymyr Baran,[b, d] Armin Kriele,[e] Martin J. Mühlbauer,[b, c] Vadim Dyadkin,[f] Alfred Rabenbauer,[g] Alexander Schökel,[d] Helmut Ehrenberg,[c] Peter Müller-Buschbaum,[a, b] and Anatoliy Senyshyn*[a, b]

A full series of variously lithiated graphite anodes material Li$_x$C$_6$ ($0 < x < 1$) corresponding to a different state-of-charge (SOC) between 0% and 100% was collected from 18650-type cylinder Li-ion batteries, and the thermal structural behavior of these electrodes was mapped using ex situ high-resolution X-ray and neutron diffraction. Their structural behavior was analyzed over a broad temperature range. At high temperatures, a non-reversible decomposition of the lithiated graphite anodes takes place, accompanied by a loss of intercalated lithium ions, forming novel phases such as LiF and Li$_2$O strongly coupled to the degradation of the solid electrolyte interface (SEI). Complementary calorimetric measurements showed the strongly exothermic chemical reactions during the decomposition matching well to the collected diffraction data. Post mortem analysis applying scanning electron microscopy revealed various morphological features supplementing the treatment of battery anodes and highlighted the importance of the SEI layer during the cycling of the cell and its thermal degradation.

Introduction

In contrast to the relatively broad choice of cathode chemistries in state-of-the-art Li-ion batteries (LIBs), graphite is the dominating anode material in all battery applications. Nowadays, graphite based anodes are the most common used negative electrode materials in commercially available LIBs. In recent years the battery volumetric capacity of pure graphite anodes with a comparable low theoretical specific capacity of 372 mAhg^{-1} has been tuned by the addition of small amounts of silicon, maintaining a higher theoretical specific capacity of 3572 mAhg^{-1} [1] and a low working potential at high safety standards and lower costs.[2] Electrochemical active graphite is ordered in a 2H configuration building up a layered hexagonal structure.[3] During electrochemical cycling, lithium ions will de-/intercalate into the graphite structure reversibly, resulting in different lithiated phases Li$_x$C$_6$ ($x < 1$) (stages), experimentally

determined by Dahn[4] and Ohzuku et al..[5] Furthermore, the stage formation in the lithiated graphite structure is defined by different d-spacings, resulting in a color change of the material from black (state-of-charge 0%) to blue (30%), red (50%) to gold (state-of-charge 100%).[6]

However, the overall performance of LIBs is still determined by the capability of graphite to store lithium ions in its structure. Additionally, the phase diagram is complex, and there are ongoing debates as well as discrepancies between the staging models at regions of small x in Li$_x$C$_6$. Furthermore, the temperature-resolved phase stability in de-/intercalated graphite is investigated poorly and controversial in the literature, as there are anomalous structural changes and inconsistencies in the temperature stability of Li$_x$C$_6$. Senyshyn et al.[7] reported that diffraction signatures between LiC$_{12}$ and graphite are different at low temperatures (300 K, 270 K, 250 K) and show structural instability. Structural anomalies and deviations of LiC$_6$, LiC$_{12}$,

[a] T. Hölderle, Prof. P. Müller-Buschbaum, Dr. A. Senyshyn
     Chair for Functional Materials, Department of Physics, TUM School of
     Natural Science
     Technical University of Munich
     James-Franck Str. 1, 85748 Garching bei München, Germany
     E-mail: anatoliy.senyshyn@frm2.tum.de

[b] T. Hölderle, Dr. M. Monchak, Dr. V. Baran, Dr. M. J. Mühlbauer,
     Prof. P. Müller-Buschbaum, Dr. A. Senyshyn
     Heinz Maier-Leibnitz Zentrum (MLZ)
     Technical University of Munich
     Lichtenbergstr. 1, 85748 Garching, Germany

[c] Dr. M. Monchak, Dr. M. J. Mühlbauer, Prof. H. Ehrenberg
     Institute for Applied Materials (IAM)
     Karlsruhe Institute of Technology (KIT)
     Hermann-von-Helmholtz-Platz 1, 76344 Eggenstein-Leopoldshafen, Germany

[d] Dr. V. Baran, Dr. A. Schökel
     Deutsches Elektronen-Synchrotron (DESY), Notkestr. 85, 22607 Hamburg,
     Germany

[e] A. Kriele
     Helmholz-Zentrum hereon GmbH
     Lichtenbergstraße 1, 85748 Garching, Germany

[f] Dr. V. Dyadkin
     Swiss-Norwegian Beamlines
     ESRF-The European Synchrotron
     Avenue des Martyrs 71, 38042 Grenoble Cedex 9, France

[g] A. Rabenbauer
     Lehrstuhl für Synthese und Charakterisierung innovativer Materialien,
     Chemie Department, TUM School of Natural Science
     Technische Universität München
     Lichtenbergstraße 4, 85748 Garching, Germany

Batteries & Supercaps

Research Article
doi.org/10.1002/batt.202300499

Chemistry
Europe

European Chemical
Societies Publishing

and deintercalated graphite have been identified by Baran et al.,[8] pointing out a thermal instability of LiC_6, which was confirmed by Cañas et al.,[9] who observed a clear difference during the de-/intercalation of lithium into graphite at ambient and higher temperatures. Furthermore, the thermal stability of lithiated graphite has been investigated in the literature using several methods like differential scanning calorimetry (DSC),[10] accelerating rate calorimetry (ARC)[11] and X-ray diffraction (XRD),[10b,12] resulting in different reported thermodynamic stabilities of intercalated lithium in the graphite structure. While Ref. [13] postulates a stable region for lithium intercalated graphite from $-25\,°C$ to $50\,°C$ Ref. [12b] investigated an unstable region from $110\,°C$ to $230\,°C$, and Ref. [12a] observed a complete degradation of intercalated graphite at $198\,°C$. Regarding the partly large discrepancy of the reported results, the investigation of the temperature-dependent structural behavior of the graphite electrode in more detail is needed in order to improve missing details regarding the stability of battery anodes, which creates a direct link to safety and capacity of the LIBs.[14] With regard to new generations of LIBs, the investigation of high-temperature stability of graphite is even more important in the scope of asymmetric temperature modulation, which is associated with extreme fast charging.[15]

In order to analyze the thermal stability of intercalated graphite in more detail, a systematic investigation combining high-resolution X-ray and neutron powder diffraction (*ex situ* and *in situ*) was carried out on various lithiated graphite samples between SOC 0% and 100%. The samples were taken from commercial available 18650-type cylindrical LIBs. The focus is set on the temperature-dependent structural evolution of the lithiated samples, combining diffraction with electrochemical data.

Experimental Section

For the studies, commercially available cylinder type cells NCR18650GA by Panasonic were chosen. These cells adopt a NCA|C cell chemistry, and their nominal capacity is 3400 mAh (experimentally determined 3350 mAh) with a nominal voltage of 3.6 V and an operation window of 2.5–4.2 V. The cells possess volumetric and gravimetric energy densities of 693 Wh/l and 224 Wh/kg, accordingly.[16] In order to activate the cells (after storage), galvanostatic cycling was executed by a Neware potentiostat in the previously mentioned voltage window applying small currents several times with constant-current constant-voltage (CCCV-Phase). The applied current was set to 400 mA (~C/8) with a cut-off current of 1% of the nominal capacity (~34 mA). To get different states-of-charges (SOCs) for each cell after cycling, charging with C/8 was applied in order to reach the specified SOC. In total 29 cells were charged to certain SOCs between 0% and 100%. After the electrochemical treatment, the cells were disassembled in a glove box (MBraun) under argon atmosphere with an oxygen level and a humidity below 2 ppm. Thus, the cylindrical cells were opened carefully to prevent short circuits, using a tube cutter along the positive terminal of the cell, followed by dismantling the steel housing, leaving the rolled stripes of electrodes and separator. The rolled stripes were taken apart and separated. A small piece of the negative electrode, located in the middle of the electrode stripe and located 15 cm from the current tab, was cut from the current collector (total length 100 cm) with a

subsequent delamination of the electrode material. The resulting material was ground in an agate mortar to a fine powder and filled into a 1 mm diameter quartz capillary sealed with 2 K epoxy glue inside the glove box. The resulting capillary was mounted on a brass pin with 2 K epoxy glue and fixed to a magnetic sample holder, further mounted on the spinner stage of beamline P02.1 at DESY.

The high-resolution and high-energy powder X-ray diffraction measurements were carried out in Debye-Scherrer geometry at beamline P02.1 at Petra III (DESY Hamburg, Germany), using a fixed photon energy of 60 keV (a monochromatic beam of $\lambda = 0.207$ Å) and a beam size adjusted to 1×1 mm^2.[17] The experimental set-up is composed of the optical elements, the diffractometer with a spinner stage for capillaries, a large area Varex XRD 4343CT (150×150 µm^2 pixel size, 2048×2048 pixel area) detector for 2D data collection with a sample to detector distance of ~2 m[18] and the sample environment. For the sample environment, an automatic sample exchange robot arm (Stäubli) with a sample magazine was used to place the capillary samples automatically on the sample spinner stage. For temperature-dependent measurements, a Cryo-stream (Oxford) with a continuous-flow cold finger cooling with liquid nitrogen was used for low temperatures (180 K–500 K), and a Hot Air Blower (HAB) (Oxford) was used for high temperatures (300 K–650 K).[17] The temperature profiles are presented in Figure S1. For the temperature calibration of the HAB, a PT100 sensor in an empty capillary placed on the sample spinner stage was used. The data acquisition time was typically set to 60 seconds per pattern due to the low scattering power of lithiated graphite. To determine instrumental contributions and peak broadening, LaB_6 (NIST SRM 660c) was measured as a reference. The collected data were integrated using the program Dioptas.[19]

In addition, a similar high-resolution *ex situ* XRD measurement has been executed at SNBL/ESRF (Grenoble, France) at the Swiss-Norwegian beamline with a wavelength of $\lambda = 0.668$ Å on a lithiated graphite anode material, collected from a fully charged real Li-ion battery of type NCR18650B (Panasonic) using a Pilatus 2 M detector. The temperature profile varied from the one used at DESY and can be seen in detail in Figure S1. Correspondingly, sample heating was applied first, ramping from ambient temperatures to 500 K. Afterwards, cooling was executed until a temperature of 105 K was reached, with the remaining beam time used to heat the material back to ambient temperatures.

High-resolution *in situ* neutron powder diffraction measurements at low temperatures were executed on fresh cylindrical lithium-ion batteries (ICR18650-26F, Samsung) adopting a LCO|C cell chemistry, a nominal capacity of 2600 mAh and a voltage window of 3.0 V–4.2 V. Cells were also charged to specific SOCs (0%, 10%, 20%, 30%, 40%, 50%, 75%, 100%) with a VMP3 Potentiostat from BioLogic. The measurements were carried out at the high-resolution instrument SPODI at beamline SR-8[20] (FRM II, Garching b. München, Germany). A combination of the monochromator take-off angle of 155° with the vertically focusing germanium monochromator (331 orientation) supplied a wavelength of $\lambda = 2.536$ Å with an incident beam size of 40×20 mm (v$\times$h) at the sample position. Data collection covered an angular range of 160° with the help of a vertically sensitive multidetector built up from 10' Soller collimators in front of 80 ^{3}He tubes with an acquisition time of 2 hours. Si SRM was used as a reference, and the instrumental resolution was determined using the profile of NAC. The samples were mounted in a top-loading closed-cycle refrigerator and studies were performed at discrete temperatures upon cooling (300 K, 270 K, 250 K, 240 K, 235 K, 230 K and 200 K).

In addition to *in situ* characterization, *ex situ* measurements have been carried out with a wavelength of $\lambda = 1.549$ Å supplied by the

Batteries & Supercaps

Research Article
doi.org/10.1002/batt.202300499

Chemistry
Europe

European Chemical
Societies Publishing

551 orientation of the vertically focusing germanium monochromator on differently lithiated graphites collected from a set of fresh commercial cylindrical lithium-ion batteries of type 18650 (Panasonic, NCR18650B) which are based on an NCA|C cell chemistry. The cells were previously charged to specific SOCs in the range of 0–100 % (in line with studies reported in Ref. [21]). In total, 26 different samples have been analyzed.

Post-mortem surface and morphology measurements were carried out quantitative and qualitative on a ThermoFisher Scientific Quattro S environmental scanning electron microscope (ESEM) operated jointly by the Helmholtz-Zentrum Hereon and Jülich Center for Neutron Science (JCNS). The scanning electron micrographs (SEM) were taken at a working distance of 12 mm with a very small probe current of 2.6 pA and an acceleration voltage of 2 kV using a standard Everhart-Thornley Detector (ETD), sensitive to secondary electrons and backscattered electrons for surface analysis. A further Thermo Fischer EDS UltraDry-Si-drift detector ($60~mm^2$) was used for energy-dispersive X-ray spectroscopy in order to analyze and map the elementary composition and distribution of the material of interest.

Thermoanalytic measurements were carried out by differential scanning calorimetry (DSC) on a Netzsch – DSC 200 F3 at the chair of synthesis and characterization of innovative materials (TUM Garching, Germany). The harvested sample material was filled in Aluminum crucibles and sealed airtight in a glove box (MBraun). The calorimetric measurements were carried out in a defined temperature range starting from 25 °C and ending at 600 °C. The temperature ramping was executed with an applied heating rate of 5 °C/min under nitrogen flow.

Results and Discussion

Low-Temperature Measurements

High-resolution X-ray measurements at DESY were conducted applying an Oxford Cryostream and starting with cooling the samples from ambient temperatures to 180 K with subsequent heating increments of 10 K. Upon cooling, thermal contraction of the lithiated phases has been observed. However, no structural changes have been identified indicating a thermodynamic stable behavior of the intercalated graphite upon low temperatures. Besides the identification of lithiated graphite phases, additional phases were observed, revealing the occurrence of long-range order reflections at low diffraction angles occurring below 325 K (Figure S2). The identified reflections are possibly dedicated to the frozen electrolyte solution, which is still present in the prepared capillary samples as well as the dried-out residues of electrolyte as $LiPF_6$ salt and EC. Such structures are observed for samples, where most of the reflections will disappear when temperatures are above 300 K. The remaining reflections are stable until 325 K. However, it was not possible to assign the observed reflections to specific phases. It is believed that the reflections correspond to electrolyte residues composed of a lithium salt ($LiPF_6$) dissolved in a mixture of, i.e., diethyl carbonate (DEC), ethyl methyl carbonate (EMC) or propylene carbonate (PC), ethylene carbonate (EC) or dimethyl carbonate (DMC).[22] The observation was rather systematic and taking place for different cell chemistries, i.e., a similar behavior was observed during measurements at ESRF.

Contrary to measurements at DESY, the heating program was carried out before cooling, starting from room temperature. Similar peaks have been observed, disappearing at 320 K, 325 K and 330 K (Figure S3). However, the melting point of each above-mentioned single solvent is lower than the highest phase transition temperature (330 K) visible in the diffraction data. For example, EC possesses the highest melting temperature at 310 K[23] among the previously mentioned solvents. This raises the question about the origin of the signals at 325 K and 330 K. As a working hypothesis, it is attributed to the preparation of the samples in the glove box, i.e., while opening the battery cell, collecting the anode material and proceeding with the further grinding process, the solvents start to evaporate and dry out. The dried residues are left on the surface of the negative electrode material (Figure S4) and can potentially be stable up to 325 K. In Ref. [24], DSC signals around 340 K were reported and attributed to the melting of dried-out EC components combined with $LiPF_6$, which would suit well to the detected reflections until 325 K and the detected endothermic signal in calorimetric measurements. At elevated temperatures, the residues may be involved in the decomposition of the solid electrolyte interface (SEI) and degradation of the lithiated anode material.

Furthermore, complementary high-resolution neutron powder diffraction measurements at low temperatures have been carried out *in situ* on cylindrical battery cells of type 18650 with LCO|C chemistry. The investigations revealed similar results to the X-ray observations. While for a SOCs between 0 % and 10 % the reflections of frozen electrolyte and the pure and lithiated graphite are overlapping, the reflection of the electrolyte becomes visible at a SOC of 10 % at 200 K and at higher SOCs. This is, because there is no pure graphite visible anymore and the reflections of lithiated graphite (i.e. $006\text{-}LiC_{30}$, $002\text{-}LiC_{12}$ and $001\text{-}LiC_6$) are shifting towards lower diffraction angles with increased SOC, while the observed electrolyte reflection remains at diffraction angles between 43° and 44° (Figure 1).

Additionally, the reflection of the electrolyte shows contraction upon cooling as it is shifted to higher diffraction angles. Note, the substantial shift of the electrolyte reflection is dedicated to the sufficiently stronger thermal contraction (typical for organic compounds when compared with inorganics). Besides this, weak electrolyte reflections were identified at roughly 25° (Figure S5). As neutrons are highly sensitive to lithiated graphite, an unusual distribution of intensities is visible for the SOCs of 10 % and 30 %, revealing overlapping reflections from different lithiated phases (LiC_{30}, LiC_{12}, Graphite), showing inhomogenieties in the graphite lithiation during the electrochemical cycle of the LIB.[25] The distribution/shape of the reflections is also changing when cooling to 200 K. However, contrary to X-ray measurements, the electrolyte reflections appear only at temperatures lower than 240 K, indicating the absence of dried-out residues (potentially related to the different ratios of irradiated volumes) and/or a different mixture of electrolyte due to a different analyzed LIB. It is important to mention that the identified signal from frozen electrolyte was found to be very similar to previously observed structural signatures of the commonly used LP30 electrolyte.[7] Further-
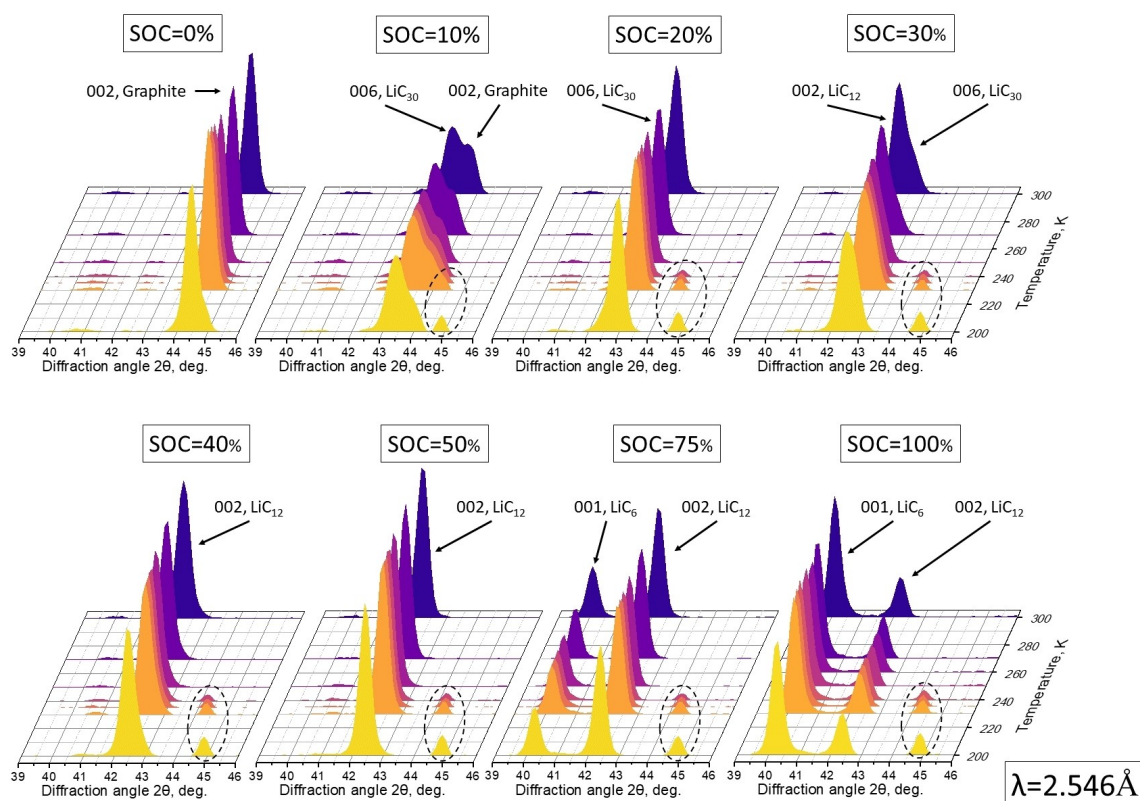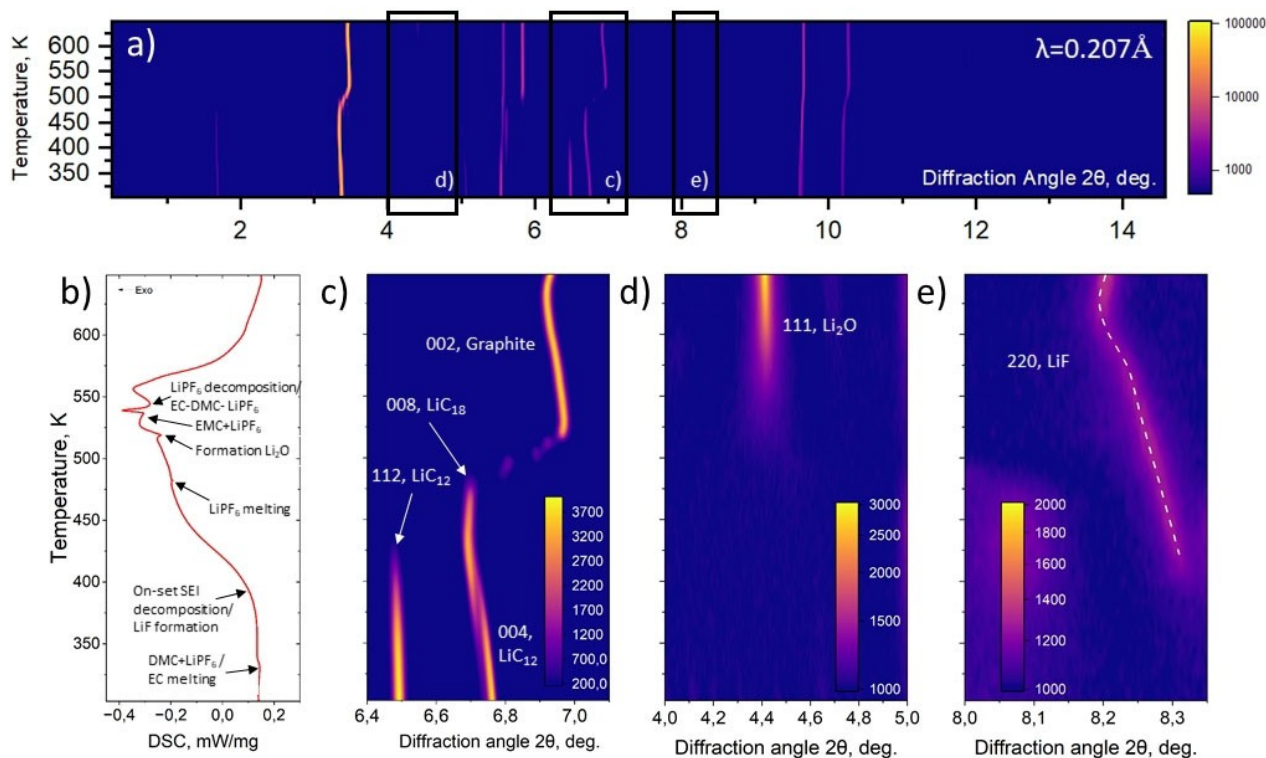
Figure 1. High-resolution neutron data collected from various SOCs showing reflection bunches of 002 reflection for graphite and LiC_{12}, 006 reflection for LiC_{30} and 001 reflection for LiC_6 with the electrolyte reflection appearing below 240 K. The origination of the electrolyte reflection and its evolution is marked by dashed ellipses.

more, the electrolyte reflections show similar behavior for all state-of-charge, indicating a state-of-charge independent behavior of the electrolyte during the electrochemical cycle of a fresh LiB. In addition to low-temperature measurements, *ex situ* studies have been executed at ambient temperatures on differently lithiated graphites in the SOC ranging from 0% to 100% in order to map the structural behavior during the electrochemical cycle. The observed diffraction signals have been found to be in good agreement with previously reported *in operando* data.[14,21,26] The 002 graphite reflection showed a shift towards lower diffraction angles upon graphite lithiation, indicating the ongoing intercalation of lithium ions from the cathode host structure into the anode graphite layers. Starting from SOC = 55%, a biphasic behavior of the structure is identified represented by the 002 reflection of LiC_{12} and the 001 reflection of LiC_6 (Figure S6). Experimental diffraction data were analyzed with Rietveld refinement using structural models of lithiated graphites proposed in Ref. [27]. The obtained evolution of weight fractions of different lithiated phases is shown in Figure S7, where a biphasic behavior of LiC_6 and LiC_{12} was observed between SOC 55% and 100%. Below SOC 55% LiC_{12} was detectable until SOC 20% and additional phases summarized as $< LiC_{12}$ (e.g. LiC_{30}) were emerging. Pure graphite was identified between SOC 0% and 10%. Unfortunately, it is not possible to achieve proper refinements below SOC 50%, as

reflected in the increase of residual factors (Figure S8). This can be attributed to several factors, where the complex behavior of low lithiated phases ($< LiC_{12}$) is the major one. It is directly reflected by the change of c lattice parameter of low lithiated phases displaying significant dependence on SOC for lithium contents $< LiC_{12}$ (Figure S9). Limited resolution and uniformity of the electrode materials are the other factors potentially affecting the data analysis.

High-Temperature Measurements

The low-temperature studies were extended to high temperatures. In Figure 2, a stack of diffraction patterns is plotted at different temperatures (using HAB) corresponding to the anode material harvested from a commercial LiB at SOC 50%, filled into a capillary under argon atmosphere, and showing first and second-order reflections of the lithiated graphite. During temperature treatment, a degradation of the lithiated graphite was observed at a certain temperature for all samples (SOCs) except pure graphite, indicating the lithium content to cause thermal instability in the real battery electrode, i.e., under the presence of the polyvinylidenfluorid (PVDF), electrolyte, ingredients of the SEI and carbon additives of the negative electrode material in commercial LIBs. The graphite delithiation at higher

Batteries & Supercaps

Research Article
doi.org/10.1002/batt.202300499

Chemistry Europe
European Chemical
Societies Publishing

Figure 2. Stack of diffraction data (a) of lithiated graphite corresponding to a SOC of 50% upon heating by HAB with (b) the corresponding DSC signal of the lithiated electrode showing DMC+LiPF$_6$/EC melting,[24,28,30] the on-set of SEI decomposition and LiF formation,[31] LiPF$_6$ melting,[29–30] formation of Li$_2$O, EMC +LiPF$_6$ peak[28] and LiPF$_6$ decomposition combined with EC-DMC-LiPF$_6$ peak[29–30] and (c) the second order reflection with its phase transition from a lithiated phase to a pure/nearly Li-free graphite phase and the formation of (d) Li$_2$O and (e) LiF phase.

temperatures has been found proceeding in different defined steps similar to the deintercalation stages of lithiated graphite anodes occurring in a commercial LIB during the electrochemical discharge[12a,27] and following LiC$_6$→LiC$_{12}$→LiC$_{18}$→Li$_x$C$_6$→Graphite (x≤0.25). However, the temperature treatment of pure graphite shows no clear phase transition as would be seen in a change of reflection intensities, but is indicated by systematic and discontinuous shifts of the reflections in addition to thermal expansion of the material, which can be seen as a continuous shift of the 002/004 reflection towards lower diffraction angles similar to measurements with the Cryostream (Figure S10a). In contrast, lowly lithiated phases show in the first stage a thermal expansion with a subsequent shift back of the 002 reflection towards higher diffraction angles, indicating a phase transition from lowly lithiated graphite phases to nearly Li-free graphite. Higher lithiated phases (SOC≥15%) display a rapid jump of the lithiated graphite reflection towards the low lithiated or Li-free graphite 002 reflection at temperatures between 400 K and 550 K. For instance, in Figure 2, representing a lithiated graphite material of SOC 50%, the 004 and 112 reflections of LiC$_{12}$ both shift in a first stage towards lower diffraction angles, which is associated with thermal expansion of the material. Simultaneously, the reflection intensity of the 112 reflection is decreasing. At a temperature of 375 K, the 112 reflection fades out, and the 004 (LiC$_{12}$) reflection is replaced by the 008 (LiC$_{18}$) reflection[27] at lower diffraction angles. A further step of degradation occurs at

temperatures around 475 K with a phase transition from LiC$_{18}$ to nearly Li-free graphite, surpassing an intermittent stages representing low lithiated phases like LiC$_{24}$ and LiC$_{30}$. From around 525 K and onwards, the graphite experiences no phase transition, but a continuous thermal expansion until the 002 reflection shifts back towards higher diffraction angles at approximately 650 K, which may be attributed to a co-intercalation of reaction products (and/or a degradation reaction with the SEI) or the reaction of residual lithium ions in the graphite structure. X-ray diffraction based investigations executed at ESRF are in good agreement with the observed degradation behavior at DESY, as the 001 reflection of the LiC$_6$ phase and the 002 reflection of the LiC$_{12}$ phase both shift towards lower diffraction angles (Figure S11), due to thermal expansion, whilst the position of the 001 reflection moves towards higher diffraction angles, thus indicating the onset of degradation. The maximum temperature reached in the experiment at ESRF was 500 K, and in fact limiting the observed degradation, followed by thermal contraction during cooling to low temperatures. Complementary to the diffraction experiments, calorimetric measurements were carried out to analyze the characteristics of the chemical reaction taking place during the elevated temperature treatment (Figure 2b). The DSC curve of the intercalated material corresponding to the SOC 50% shows a broad exothermic reaction pathway with a number of small endothermic peaks on top. The onset of the broad DSC anomaly is at 374 K is matching quite well with the taken

diffraction data and corresponds mainly to the degradation of LiC_{12} into nearly Li-free graphite, accompanied by reactions with SEI and electrolyte components. Thus, the growing exothermic peak describes the chemical reaction of intercalated lithium causing its disappearance from the graphitic host structure until a temperature of 525 K is reached. Afterward, further reactions related to the SEI and the electrolyte can be attributed to several peaks, which may be associated with degradation mechanisms dedicated to the SEI breakdown and electrolyte mixture: According to Ref. [28], an electrolyte mixture of DMC and $LiPF_6$ salt shows an endothermic peak occurring at 340 K and is visible in Figure 2, while a mixture of EC and $LiPF_6$ shows an exothermic peak at 485 K, not visible in the DSC signal. However, a typical electrolyte mixture is composed of EC, DMC, $LiPF_6$, and possibly other solvents such as DEC, EMC or PC.[22] Such a mixture of multiple solvents will show multiple alternating endothermic and exothermic peaks at elevated temperatures, as it is observed in Figure 2,[28–29] making it difficult to assign the peaks to a specific electrolyte composition, which remained unknown for the analyzed commercial cell. At temperatures of 480 K and 536 K further small endothermic peaks are observed dedicated to the melting of the $LiPF_6$ salt according to Ref. [29–30], followed by the maximum of the internal energy released. At a temperature of 538 K a subsequent decrease of the huge exothermic peak was observed. The temperature cut-off of the huge exothermic peak is identified at 643 K followed by additional exothermic and endothermic signals, potentially associated with co-intercalation

phenomena. However, as seen in Figure 2, the exothermic reaction continues even after the graphite phase has evolved. This can be related to the strong exothermic behavior at elevated temperatures caused by the SEI degradation and its self-healing reactions.[11a,30] Thus, the observed strongly exothermic reaction is not only dedicated to the degradation reactions of the intercalated lithium but also to chemical reactions dedicated to the SEI layer and the electrolyte. Note, the magnitude of the DSC signal has been found to increase with increasing SOC (Figure S12), while the starting temperatures of the exothermic reaction are quite similar for all SOCs. In contrast, the cut-off temperatures have been found to increase for higher SOCs (Figure S13), which is in line with the increased enthalpy of the monitored reactions (Figure S14). The observed trend represents an increasing degradation chain from high to lowly lithiated and delithiated (pure/nearly Li-free) graphite coupled with a degradation of the electrode (in terms of composition, morphology and additives). It is important to notice that the degradation is happening not only at a specific SOC, but over the entire bandwidth of SOCs, which may be best visualized by Figure 3, showing the interatomic distribution of d-spacings (for the sake of comparison) at 300 K before and after high-temperature treatment. The measured d-spacings can be divided into three different regions, representing different SOC and degree of lithiation in graphite. In region 1 (0%–15% SOC) the d-spacing is represented by the 002 reflection (first order) and 004 reflection (second order) of graphite corresponding to the lowest possible d-spacing for
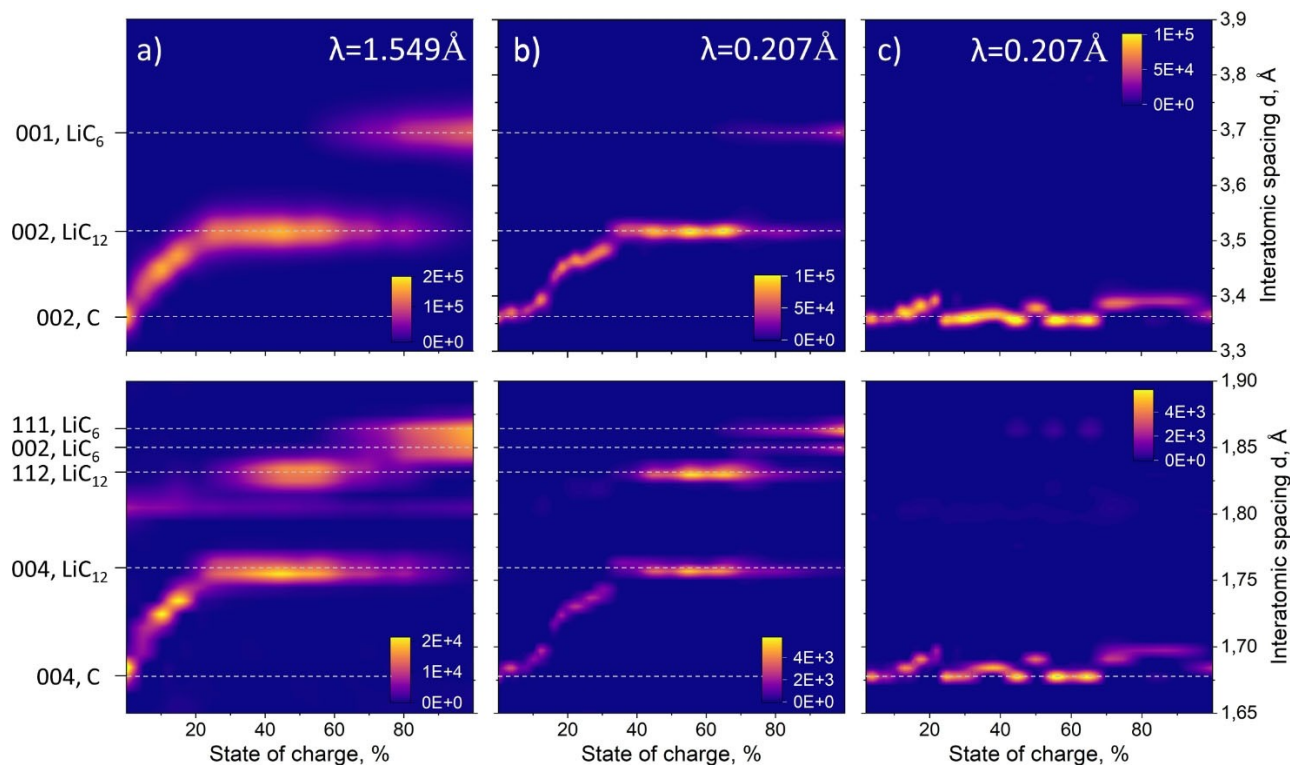
Figure 3. Interatomic spacing d for a) results from neutron powder diffraction (NNP cell) showing first (upper row) and second order reflections (lower row) of 00L type and for high-energy X-Ray diffraction measurements b) before temperature treatment at 300 K and c) after temperature treatment at 300 K. White lines are guides for the eyes and show a constant interatomic spacing d after temperature treatment.

Batteries & Supercaps

Research Article
doi.org/10.1002/batt.202300499

Chemistry Europe
European Chemical
Societies Publishing

intercalated graphite. Region 2 (15%–40% SOC) is characterized by a steep increase in d-spacing, which is related to the change from lowly lithiated graphite to the LiC_{30} phase. In region 3 a biphasic behavior of LiC_{12} and LiC_6 coexisting at higher SOC is visible.

After temperature treatment and subsequent cooling of the samples back to 300 K, the observed diffraction patterns are very similar regardless of the initially different samples/SOCs, indicating non-reversible structural changes. A closer inspection reveals the diffraction patterns of heat-treated samples to be similar to that of Li-free graphite, which may correspond to temperature- resolved delithiation from lithiated graphites. This hypothesis was further cross checked by the analysis of the temperature-dependent c lattice parameter behavior. The drastic shrinkage between carbon honeycomb planes gives strong evidence for such a reaction (Figure S15).

The observed degradation mechanism displays well-resolved kinetic behavior, requiring to include time as a parameter. A series of isothermal experiments has been performed on another lithiated graphite sample, corresponding to 50% SOC (Figure S16), where the temperature was increased to predefined specific temperatures, starting at 448 K with a subsequent annealing period of 15 minutes. In the first temperature step, no changes in the structure have been observed at all. However, in contrast to the previous sample (SOC 50%), the additional phase LiC_{30} was detected. After increasing the temperature to 456 K, differences in intensities were observed, attributed to increased temperatures. No further change was detected for longer waiting periods, so that equilibrium conditions seem to be reached. When increasing the temperature to 464 K, the subsequent annealing of 30 minutes showed an apparent decrease in intensity of the LiC_{12} 112 and LiC_{30} 106 reflection. After a further increase of the temperature to 472 K and an annealing time of 20 minutes, the reflections of the lithiated graphite reflections showed degradation of their structure, visible by the decreasing intensity of the LiC_{12} 004 reflection, resulting in the appearance of lowly lithiated graphite reflections. Thus, by further heating to 480 K, graphite reflection intensities 004 and 103 started to increase. The structure was stabilizing after a temperature of 488 K was reached, showing that besides the temperature, time is another criterion to be considered in the degradation of intercalated graphites, where an increasing temperatures will speed up delithiation and facilitate the reaction to a nearly Li-free graphite structure.

However, besides the observed degradation of intercalated graphites, there is a number of other effects supplementing the losses of intercalated lithium ions. In the closed system, lithium ions are not able to vanish, i.e., they will leach and react together with other electrode\cell components like the PVDF binder, carbon black as well as the decomposition products of the SEI, present in the battery anodes, as shown in the following reactions.

$$4\ Li^+ + 4e^- + O_2\ \rightarrow 2\ Li_2O$$

$$2\ Li^+ + 2e^- + F_2\ \rightarrow 2\ LiF$$
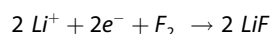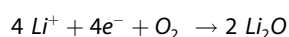
Diffraction signals from the Li_2O and LiF phases were detected at higher temperatures (see Figure 2 for details), which were also found stable after the high-temperature treatment (room temperature). Li_2O was detected for all high-temperature measurements executed with the HAB, originating at temperatures between 500 K and 550 K and observed by the 111 reflection (Figure S17), where its intensity has been found to increase with increasing temperatures. The Li_2O formation was observed in calorimetric measurements as an endothermic peak at 525 K (Figure 2b). Simultaneously, the reflection intensity 220 of the LiF phase was observed already at temperatures between 375 K and 400 K (Figure S18). No characteristic signal from LiF formation was observed in the calorimetry data. However, it can be associated with the onset of the broad exothermic peak and in good agreement with the degradation of the SEI at 390 K, as discussed in Ref. [31]. The observed phases are products of several reactions associated with the temperature-dependent degradation of the PVDF binder, carbon black and the SEI layer,[32] directly affecting specific aging mechanisms in LIBs. One can consider the SEI as a thin layer on the surface of carbon/graphite grains in the anode, maintaining high ionic conductivity/Li-ion selectivity along with an electrical insulation property.[33] Its chemical composition largely resembles the reduction products of the electrolyte (a mixture of aprotic polar solvents such as DMC and EC combined with lithium salts, e.g., $LiPF_6$.[34]) resulting in multiple decomposition products, i.e., inorganic salts like lithium oxides, metastable organic parts R-OCO_2Li, R-OLi (R = alkyl group), lithium ethylene di-carbonate and poly(ethylene oxide) (PEO) oligomer[12a,35] etc. When the temperature is increased to 328 K, parts of the SEI start to degrade,[36] and the lithium oxides decompose together with the lithium salt $LiPF_6$ in the presence of DMC to primarily gaseous CO_2 and crystalline LiF. No diffraction signatures of LiF were observed at these temperatures. However, besides LiF formation, the SEI undergoes a variety of decomposition reactions,[37] potentially resulting in lithium ions leaching from the carbon particle and reacting with either the electrolyte to form fresh SEI layer[30] or with the decomposing PVDF binder, supplying, in turn, fluoride ions to form LiF during the release of H_2 gas at 375–400 K.[12a,38] The formation of the LiF phase is followed by the formation of the Li_2O compound starting at temperatures above 500 K. Also, lithium from the SEI layer and molten lithium from the graphite particles may react with the available oxygen to form Li_2O.[39] Alternatively, Li_2O may be formed by the reaction of lithium, H_2O and/or CO_2 delivered by the decomposition of PEO oligomers.[35b] Density functional theory based modeling[40] displayed the tendency towards the decomposition of the PEO oligomer to produce Li_2O together with lithium ions. According to Ref. [12a,] the decomposition was experimentally observed using diffraction, based on reflection intensities arising for d-spacings between 3.9 Å–4.05 Å, whilst the intensities of reflections related to the PEO oligomer – related reflections has been found decreasing with increasing temperature and shifting towards lower

Batteries & Supercaps

Research Article
doi.org/10.1002/batt.202300499

Chemistry Europe
European Chemical
Societies Publishing

diffraction angles due to thermal expansion (Figure S19). The breakdown of the PEO oligomer is reached at a temperature of 330 K, marked by the disappearance of the reflection. Thus, the degradation of the lithium intercalated graphite structure and the corresponding reduction of active lithium as well as the vanishing of lithiated phases is strongly dependent on temperature, the complex decomposition behavior of the SEI and its interaction with the electrolyte. While *ex situ* investigations can be handled in a safe and controlled environment, the cycling of a real battery that would reach such elevated temperatures i.e. during fast charging will represent a serious hazard. Thus, the danger of thermal runway and the loss of active lithium inside the cell are limiting nowadays the usage of Li-ion batteries for fast charging applications.

Morphological Characterizations

Post mortem investigations were carried out in order to analyze the morphological impact of thermal degradation and electrochemical cycling to the lithiated electrode material. The lithiated graphite is highly sensitive to humidity and air exposure, as the intercalated lithium can react easily with oxygen and humidity.[39] Furthermore, the chemical compounds of the SEI are known to bind CO_2 and moisture to form reduction products such as lithium oxide and lithium hydroxide.[41] Such interaction was observed during air exposure measurements (Figure S20), where morphological differences of the surface and quantitative changes in the amount of oxygen were observed, indicating a continuous growth of reduction products on the surface of the graphite electrode, while exposed to the air. Thus, an airtight container similar to the one used in Ref. [42] was used to transfer the sensitive samples from the argon atmosphere in the glovebox into the SEM. The transfer container was made up from an aluminum base with a cover, separated by a sealing ring and a latex rubber membrane (Figure S21). When placed in the SEM chamber, the membrane gets expanded by the pressure difference between evacuated chamber and argon-filled transfer cell until it touches a needle, placed on the top of the module, leading to the bursting of the membrane. After evacuation of remaining argon the scanning with electron beam can be performed on air-sensitive samples.

In a fully discharged state the graphite sample consists of graphite flakes with a smooth surface, whilst at a SOC of 50% a different surface is observed. Graphite flakes can be identified, but the reaction products containing oxygen (according to EDX measurements) passivates the graphite surface. The amount of oxygen - rich products further increases at a fully charged state. Besides the continuously growing SEI layer (visible on the surface of the graphite in the SEM images as seen in Figure S22[43]), the observed behavior can be associated with the oxidation of the solvent blend gradually increasing with an increasing cell potential. Furthermore, EDX measurements revealed the occurrence of fluorine in high amounts on the surface of the graphite grain, which may be linked to the formation of the LiF phase as a major component of the SEI layer. A similar behavior was observed for thermally treated

samples (HAB), whose surface was coated with degradation products (similar to the configuration at SOC 100%). In order to illustrate such a problem, SEM data were taken on a fresh lithiated piece of electrode at SOC 100% and on a temperature treated anode, taken after XRD measurements at DESY. For an untreated anode the graphite flakes are clearly visible in the presence of reduction products, whilst for a temperature treated anode no isolated flakes could be resolved (Figure S23). The EDX measurements revealed oxygen as the main component of the surface, combined with small amounts of fluorine and phosphorus.
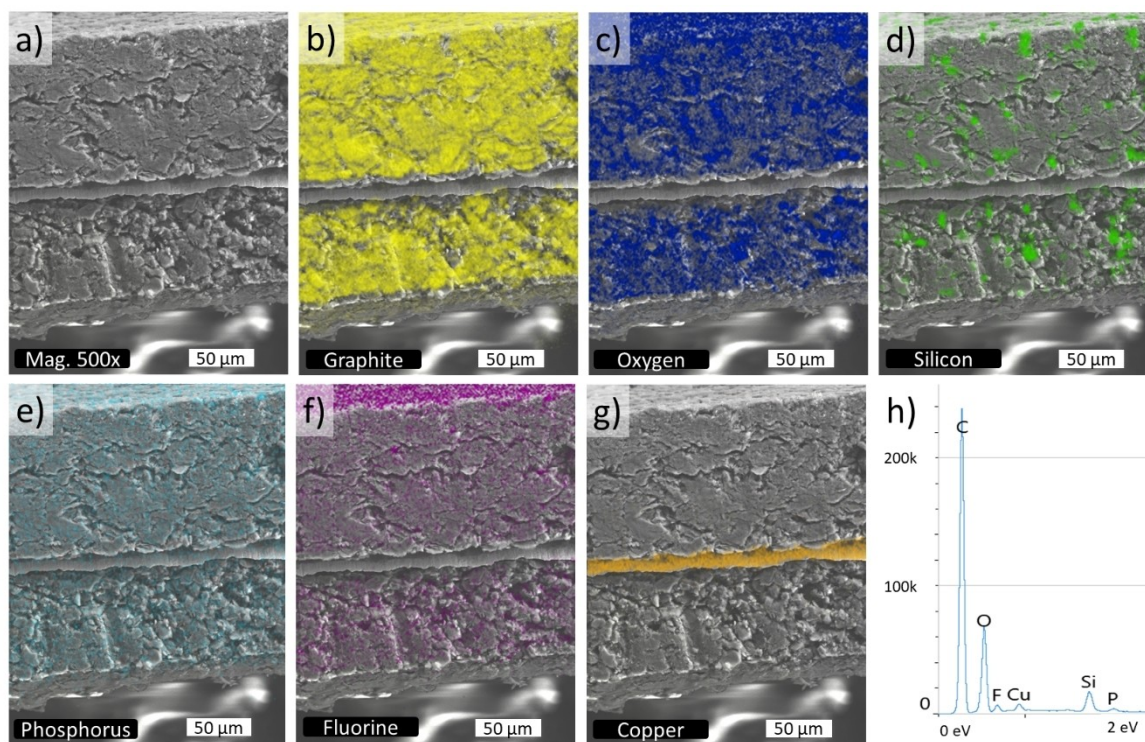
Besides the degradation-driven passivation layers on the graphite surface, silicon was identified in the graphite anode of ICR18650GA (Panasonic) cells. It was not observed in the XRD data, possibly indicating its amorphous form typically occurring after cell formation.[44] In order to map the amount of silicon, an EDX measurement (Table S1) was carried out with low magnification (1200x) on the surface of a lithiated graphite corresponding to 50% SOC. Its surface was cleaned previously with DMC to get rid of unwanted residues at the anode surface. The amount of silicon was determined to be 3%w/w corresponding to a low silicon – content anode.[45] Furthermore, the cross section of the negative anode of the battery cell (Figure 4) clearly reveals a copper current collector with silicon-graphite composites on its sides with silicon equally distributed within the anode layers.

It is worth to be mentioned, that while the graphite, the silicon and the oxygen are equally distributed throughout the anode, the fluorine signal is dominant at the outer surface of the anode (close to the separator), potentially reflecting an occurrence of LiF at the electrolyte/electrode interface. The LiF is a reduction product of fluorinated salts such as $LiPF_6$,[46] whose precipitation on the anode surface is a product of the electrolyte decomposition.

Conclusions

The thermal degradation was investigated for a series of lithiated graphites corresponding to different states-of-charge (SOC = 0–100%) by a combination of *ex situ* diffraction methods at low and high temperatures, calorimetry and scanning electron microscopy. The material was harvested from real LIBs of 18650 type at predefined SOCs, where the cells were taken apart under argon atmosphere and the material was processed for the investigations. At low temperatures, no degradation of the lithiated material was recognized except minor changes of reflection intensities in the neutron experiment together with the appearance of additional reflections from the frozen electrolyte components during in situ characterizations of 18650-type cells at various SOCs. High temperature studies revealed an ongoing degradation of the lithiated graphite starting at temperatures around 350 K, which is very close to the upper operational temperature range of state-of-the-art LIBs. Delithiation occurs at elevated temperatures for lithiated graphites over the entire range of SOC, where the degradation is kinetically controlled by the temperature level. Calorimetric studies show the complex character of the degradation

Batteries & Supercaps

Research Article
doi.org/10.1002/batt.202300499

Chemistry Europe
European Chemical
Societies Publishing

Figure 4. Cross section of the negative electrode (SOC = 100 %) measured with an ETD detector (a) and with an EDX detector showing the distribution of (b) graphite (yellow), (c) oxygen (blue), (d) silicon (green), (e) fluorine (purple), (f) phosphorus (cyan), (g) copper (orange) along with EDX results summarized in (h). More details can be found in the Supplementary Information (Figure S24).

involving the PVDF binder, electrolyte residues and the decomposition of intercalated graphite. At temperatures above 375 K a formation of Li_2O and LiF in real battery anodes was revealed by XRD. SEM investigations of the electrode morphology were performed and displayed different modes of surface passivation due to (i) air contamination, (ii) high temperature treatment and (iii) varying SOC. EDX unambiguously revealed silicon in ~3 % w/w, which was not confirmed by diffraction possibly indicating its amorphous nature.

In summary, a complex and non-trivial behavior of the lithiated anode's thermal stability in real-life batteries was observed, being a critical factor in terms of fast charging and discharging, which shifts the operational thermal window of commercial batteries towards higher temperatures due to the increased Joule's heating of LIBs and thereby raising the risk of thermal runway. Improved kinetics and elevated diffusion enables the application of higher currents sufficiently increasing the cell performance. However, counteracting to these advantages, a faster cell degradation takes place at elevated temperatures, where the thermal instability of the anode is one of the major reasons. To tackle this problem, a consolidated approach including an optimization of the high-temperature stability of binder and electrolyte may be required.

Conflict of Interests

The authors declare no conflict of interest.

Data Availability Statement

The data that support the findings of this study are available from the corresponding author upon reasonable request.

[1] a) P. U. Nzereogu, A. D. Omah, F. I. Ezema, E. I. Iwuoha, A. C. Nwanya, *Appl. Surf. Sci. Adv.* **2022**, *9*, 100233; b) S. He, S. Huang, S. Wang, I. Mizota, X. Liu, X. Hou, *Energy Fuels* **2021**, *35*, 944–964; c) J. Yu, M. Jiang, W. Zhang, G. Li, R. A. Soomro, N. Sun, B. Xu, *Small Methods* **2023**, *7*, 2300708.

[2] a) M. Endo, C. Kim, K. Nishimura, T. Fujino, K. Miyashita, *Carbon* **2000**, *38*, 183–197; b) S. Goriparti, E. Miele, F. De Angelis, E. Di Fabrizio, R. Proietti Zaccaria, C. Capiglia, *J. Power Sources* **2014**, *257*, 421–443.

[3] P. Trucano, R. Chen, *Nature* **1975**, *258*, 136–137.

[4] J. R. Dahn, *Phys. Rev. B* **1991**, *44*, 9170–9177.

[5] T. Ohzuku, Y. Iwakoshi, K. Sawai, *J. Electrochem. Soc.* **1993**, *140*, 2490.

[6] A. Shellikeri, V. Watson, D. Adams, E. E. Kalu, J. A. Read, T. R. Jow, J. S. Zheng, J. P. Zheng, *J. Electrochem. Soc.* **2017**, *164*, A3914.

[7] A. Senyshyn, M. J. Mühlbauer, O. Dolotko, H. Ehrenberg, *J. Power Sources* **2015**, *282*, 235–240.

[8] V. Baran, O. Dolotko, M. J. Mühlbauer, A. Senyshyn, H. Ehrenberg, *J. Electrochem. Soc.* **2018**, *165*, A1975.

[9] N. A. Cañas, P. Einsiedel, O. T. Freitag, C. Heim, M. Steinhauer, D.-W. Park, K. A. Friedrich, *Carbon* **2017**, *116*, 255–263.

[10] a) O. Haik, S. Ganin, G. Gershinsky, E. Zinigrad, B. Markovsky, D. Aurbach, I. Halalay, *J. Electrochem. Soc.* **2011**, *158*, A913; b) M. Drüe, M. Seyring, A. Kozlov, X. Song, R. Schmid-Fetzer, M. Rettenmayr, *J. Alloys Compd.* **2013**, *575*, 403–407; c) A. M. Andersson, K. Edström, J. O. Thomas, *J. Power Sources* **1999**, *81–82*, 8–12; d) V. V. Avdeev, A. P. Savchenkova, L. A. Monyakina, I. V. Nikol'skaya, A. V. Khvostov, *J. Phys. Chem. Solids* **1996**, *57*, 947–949.

[11] a) M. N. Richard, J. R. Dahn, *J. Electrochem. Soc.* **1999**, *146*, 2068; b) J. Jiang, J. R. Dahn, *Electrochim. Acta* **2004**, *49*, 4599–4604.

[12] a) X. Liu, L. Yin, D. Ren, L. Wang, Y. Ren, W. Xu, S. Lapidus, H. Wang, X. He, Z. Chen, G.-L. Xu, M. Ouyang, K. Amine, *Nat. Commun.* **2021**, *12*, 4235; b) Z. Chen, Y. Qin, Y. Ren, W. Lu, C. Orendorff, E. P. Roth, K. Amine, *Energy Environ. Sci.* **2011**, *4*, 4023–4030.

[13] V. Pande, V. Viswanathan, *Phys. Rev. Mater.* **2018**, *2*, 125401.

[14] A. Senyshyn, O. Dolotko, M. J. Mühlbauer, K. Nikolowski, H. Fuess, H. Ehrenberg, *J. Electrochem. Soc.* **2013**, *160*, A3198.

[15] X.-G. Yang, T. Liu, Y. Gao, S. Ge, Y. Leng, D. Wang, C.-Y. Wang, *Joule* **2019**, *3*, 3002–3019.

[16] W. Diao, C. Kulkarni, M. Pecht, *Energies* **2021**, *14*, 5434.

[17] A.-C. Dippel, H.-P. Liermann, J. T. Delitz, P. Walter, H. Schulte-Schrepping, O. H. Seeck, H. Franz, *J. Synchrotron Radiat.* **2015**, *22*, 675–687.

[18] A. Schokel, M. Etter, A. Berghauser, A. Horst, D. Lindackers, T. A. Whittle, S. Schmid, M. Acosta, M. Knapp, H. Ehrenberg, M. Hinterstein, *J. Synchrotron Radiat.* **2021**, *28*, 146–157.

[19] C. Prescher, V. B. Prakapenka, *High Pressure Res.* **2015**, *35*, 223–230.

[20] a) M. Hoelzel, A. Senyshyn, O. Dolotko, *JLSRF* **2015**, *1*; b) M. Hoelzel, A. Senyshyn, N. Juenke, H. Boysen, W. Schmahl, H. Fuess, *Nucl. Instrum. Methods Phys. Res. Sect. A* **2012**, *667*, 32–37; c) R. Gilles, M. Hoelzel, M. Schlapp, F. Elf, B. Krimmer, H. Boysen, H. Fuess, in *Ninth European Powder Diffraction Conference*, Oldenbourg Wissenschaftsverlag, **2015**, pp. 183–188.

[21] T. Hölderle, M. Monchak, V. Baran, O. Dolotko, S. Bette, D. Mikhailova, A. Voss, M. Avdeev, H. Ehrenberg, P. Müller-Buschbaum, A. Senyshyn, *J. Power Sources* **2023**, *564*, 232799.

[22] Q. Li, J. Chen, L. Fan, X. Kong, Y. Lu, *Green Energy & Environ.* **2016**, *1*, 18–42.

[23] B. Flamme, G. Rodriguez Garcia, M. Weil, M. Haddad, P. Phansavath, V. Ratovelomanana-Vidal, A. Chagnes, *Green Chem.* **2017**, *19*, 1828–1849.

[24] H. Maleki, G. Deng, A. Anani, J. Howard, *J. Electrochem. Soc.* **1999**, *146*, 3224.

[25] a) M. J. Mühlbauer, D. Petz, V. Baran, O. Dolotko, M. Hofmann, R. Kostecki, A. Senyshyn, *J. Power Sources* **2020**, *475*, 228690; b) A. Senyshyn, M. J. Mühlbauer, O. Dolotko, M. Hofmann, H. Ehrenberg, *Sci. Rep.* **2015**, *5*, 18380.

[26] a) A. Senyshyn, V. Baran, M. J. Mühlbauer, M. Etter, M. Schulz, K. Tu, Y. Yang, *ACS Appl. Energ. Mater.* **2021**, *4*, 3110–3117; b) O. Dolotko, A. Senyshyn, M. J. Mühlbauer, K. Nikolowski, H. Ehrenberg, *J. Power Sources* **2014**, *255*, 197–203.

[27] C. Didier, W. K. Pang, Z. Guo, S. Schmid, V. K. Peterson, *Chem. Mater.* **2020**, *32*, 2518–2531.

[28] Q. Wang, J. Sun, C. Chen, *Rare Met.* **2006**, *25*, 94–99.

[29] A. D. Pasquier, F. Disma, T. Bowmer, A. S. Gozdz, G. Amatucci, J. M. Tarascon, *J. Electrochem. Soc.* **1998**, *145*, 472.

[30] J. Hou, M. Yang, D. Wang, J. Zhang, *Adv. Energy Mater.* **2020**, *10*, 1904152.

[31] D. Aurbach, A. Zaban, Y. Ein-Eli, I. Weissman, O. Chusid, B. Markovsky, M. Levi, E. Levi, A. Schechter, E. Granot, *J. Power Sources* **1997**, *68*, 91–98.

[32] S. Huang, L.-Z. Cheong, D. Wang, C. Shen, *Appl. Surf. Sci.* **2018**, *454*, 61–67.

[33] E. Peled, *J. Electrochem. Soc.* **1979**, *126*, 2047.

[34] a) P. Ganesh, P. R. C. Kent, D.-e. Jiang, *J. Phys. Chem. C* **2012**, *116*, 24476–24481; b) R. Fong, U. von Sacken, J. R. Dahn, *J. Electrochem. Soc.* **1990**, *137*, 2009.

[35] a) P. Verma, P. Maire, P. Novák, *Electrochim. Acta* **2010**, *55*, 6332–6341; b) S. J. An, J. Li, C. Daniel, S. Mohanty, S. Nagpure, D. L. Wood, *Carbon* **2016**, *105*, 52–76; c) A. L. Michan, M. Leskes, C. P. Grey, *Chem. Mater.* **2016**, *28*, 385–398; d) J. E. Owejan, J. P. Owejan, S. C. DeCaluwe, J. A. Dura, *Chem. Mater.* **2012**, *24*, 2133–2140.

[36] B. S. Parimalam, A. D. MacIntosh, R. Kadam, B. L. Lucht, *J. Phys. Chem. C* **2017**, *121*, 22733–22738.

[37] A. Kriston, I. Adanouj, V. Ruiz, A. Pfrang, *J. Power Sources* **2019**, *435*, 226774.

[38] X. Zhao, S. Niketic, C.-H. Yim, J. Zhou, J. Wang, Y. Abu-Lebdeh, *ACS Omega* **2018**, *3*, 11684–11690.

[39] V. Etacheri, R. Marom, R. Elazari, G. Salitra, D. Aurbach, *Energy Environ. Sci.* **2011**, *4*, 3243–3262.

[40] A. Mirsakiyeva, M. Ebadi, C. M. Araujo, P. Brandell, P. Broqvist, J. Kullgren, *J. Phys. Chem. C* **2019**, *123*, 22851–22857.

[41] a) D. Aurbach, Y. Cohen, *J. Electrochem. Soc.* **1996**, *143*, 3525; b) D. Aurbach, A. Zaban, *J. Electroanal. Chem.* **1993**, *348*, 155–179; c) O. Chusid, E. Ein Ely, D. Aurbach, M. Babai, Y. Carmeli, *J. Power Sources* **1993**, *43*, 47–64; d) D. Aurbach, K. Gamolsky, B. Markovsky, Y. Gofer, M. Schmidt, U. Heider, *Electrochim. Acta* **2002**, *47*, 1423–1439.

[42] R. M. Gaume, L.-M. Joubert, *Rev. Sci. Instrum.* **2011**, *82*, 123705.

[43] a) V. A. Agubra, J. W. Fergus, *J. Power Sources* **2014**, *268*, 153–162; b) D. Zane, A. Antonini, M. Pasquali, *J. Power Sources* **2001**, *97–98*, 146–150.

[44] a) J. Li, J. R. Dahn, *J. Electrochem. Soc.* **2007**, *154*, A156; b) M. N. Obrovac, V. L. Chevrier, *Chem. Rev.* **2014**, *114*, 11444–11502.

[45] a) J. Moon, H. C. Lee, H. Jung, S. Wakita, S. Cho, J. Yoon, J. Lee, A. Ueda, B. Choi, S. Lee, K. Ito, Y. Kubo, A. C. Lim, J. G. Seo, J. Yoo, S. Lee, Y. Ham, W. Baek, Y.-G. Ryu, I. T. Han, *Nat. Commun.* **2021**, *12*, 2714; b) G. E. Blomgren, *J. Electrochem. Soc.* **2017**, *164*, A5019.

[46] a) D. Aurbach, Y. Ein-Ely, A. Zaban, *J. Electrochem. Soc.* **1994**, *141*, L1; b) D. Aurbach, *J. Power Sources* **2003**, *119–121*, 497–503.